ADVANCED MATERIALS TECHNOLOGIES
www.advmattechnol.de

Innervation of Sensing Microchannels for Three-Dimensional Stimuli Perception

*Dongliang Fan, Renjie Zhu, Xin Yang, Hao Liu, Ting Wang, Peisong Wang, Wenyu Wu, Huacen Wang, Yunteng Ma, Jian S. Dai, and Hongqiang Wang**

Stimuli perception enables animals and robots to interact with unknown environments safely and predictably. For the sensing of soft robotics and wearable devices, although electronic skins have already been widely accepted and studied, their planar geometries are not applicable for multi-direction volume sensing. Herein, the innervation of sensing microchannel networks into elastic matrices to mimic the exteroception and proprioception of the human bodies is employed. Soft actuators with interlaced actuating and sensing microchannels resembling the distribution of muscle fiber and proprioceptors are fabricated and the internal stimuli perception of deformation configurations (bending, elongating, and bending directions) and magnitudes (bending angle and elongation) of the soft actuators are demonstrated. It is also demonstrated that a soft cubic sensor containing 3D microchannels (diameter: 400 µm) is capable of identifying 3D external stimuli, including force types (pressing, squeezing, shearing, and twisting) and real-time directions by measuring the resistance variation, and its application in the virtual reality field is exhibited.

1. Introduction

Perception is critical for biological systems' compatibility in the unknown environment by receiving external and internal stimuli. The distributed mechanoreceptors in skins endow our bodies with exteroception to identify pressing, touching, and shearing,[1] and the innervation of proprioceptors around skeletal muscles enables proprioception for movement with high precision.[2] Soft robots and wearable devices have recently exhibited tremendous potential in human–machine interaction due to their compliant structures for adaptive interactions[3–6] and matched sensing systems for close-loop controls.[7–10] More complex configurations and functional structures are employed for these soft machines to achieve more sophisticated tasks. However, the complex structures result in difficulties in arranging soft sensors for multimodal perceptions, which is critical for robots to interact safely and predictably with unknown environments. Existing electronic skins, including resistive-type and capacitive-type, have been developed through different approaches, including thin buckling silicon,[11] carbon nanotubes,[12] and silver nanowires,[13] to achieve exteroception and proprioception for soft robotics or wearable devices by attaching artificial skins on end effectors[14] and joints[15] respectively, and demonstrated their versatile sensing abilities for complicated tasks, such as recognizing different types and directions of mechanical stimuli on surfaces,[16–20] and conformally contacted with unstructured objects, such as prosthetic hands[11] and medical catheters.[21] Still, these artificial skins require sophisticated fabrication processes[11] and specific materials,[19] and their planar geometries are not sufficient for precepting complex internal or external stimuli of 3D soft robotics and intelligent structures.[22–24]

Recently, encapsulating conducting liquids into elastomers via embedded channel structures has become a popular method for soft sensor fabrication due to the highly compliant structures and low-cost, simple fabrication processes.[25–27] However, this resistive sensor lacks the sensibility for complex external stimuli, including shearing and twisting, and force direction recognition due to their 2D patterns. Although efforts, such as introducing a rigid part[26] and configuration design,[28,29] have been made for shear force and force direction recognition, the flat ge-

D. Fan, R. Zhu, X. Yang, H. Liu, T. Wang, H. Wang, Y. Ma, J. S. Dai, H. Wang
Shenzhen Key Laboratory of Biomimetic Robotics and Intelligent Systems
Department of Mechanical and Energy Engineering
Southern University of Science and Technology
Shenzhen, Guangdong 518055, P. R. China
E-mail: wanghq6@sustech.edu.cn

D. Fan, R. Zhu, X. Yang, H. Liu, P. Wang, H. Wang, Y. Ma, H. Wang
Guangdong Provincial Key Laboratory of Human-Augmentation and Rehabilitation Robotics in Universities
Southern University of Science and Technology
Shenzhen, Guangdong 518055, P. R. China

W. Wu
School of System Design and Intelligent Manufacturing
Southern University of Science and Technology
Shenzhen, Guangdong 518055, P. R. China

J. S. Dai
Centre for Robotics Research
Department of Engineering
King's College London
Strand, London WC2R 2LS, UK

H. Wang
Southern Marine Science and Engineering Guangdong Laboratory (Guangzhou)
Guangzhou 510000, P. R. China

The ORCID identification number(s) for the author(s) of this article can be found under https://doi.org/10.1002/admt.202300185

DOI: 10.1002/admt.202300185

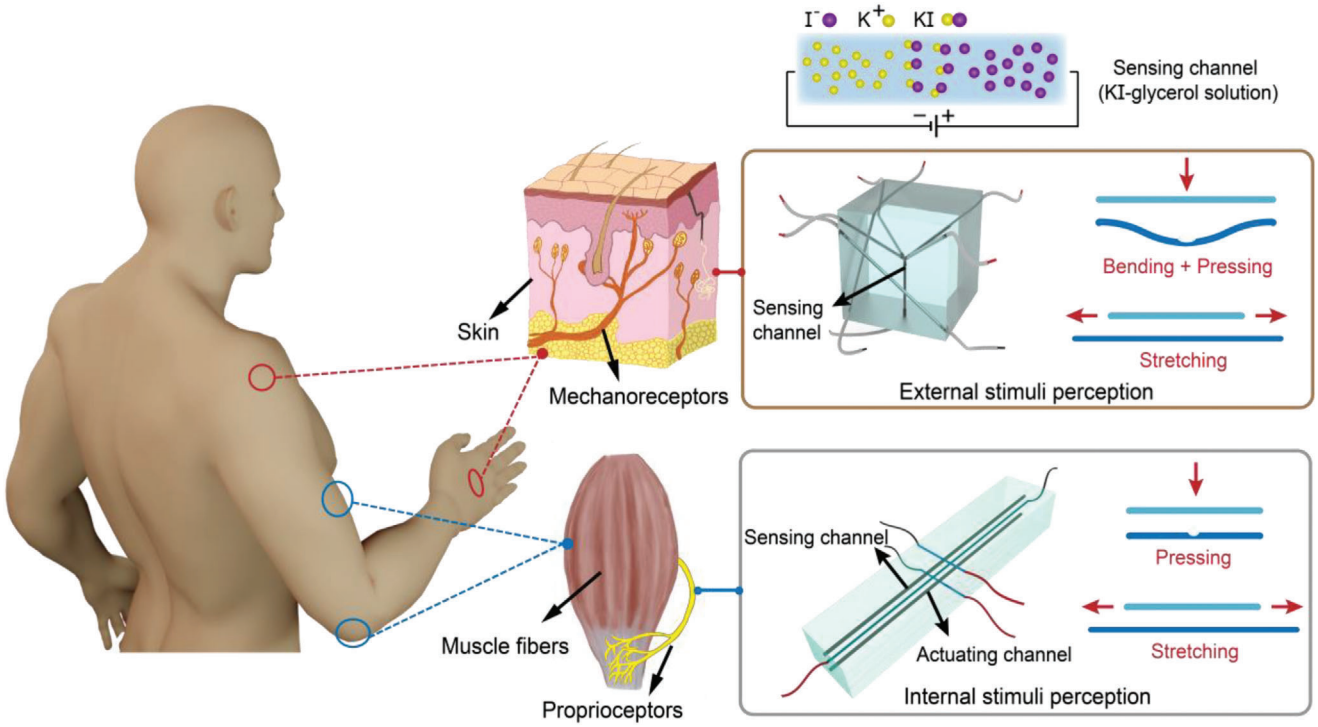

Figure 1. Innervation of sensing channels for external and internal stimuli perception and the conducting mechanism of the sensing channel.

ometries are unable to attach to uneven surfaces conformally. Moreover, embedded soft sensors into soft robotics have presented a potential solution to proprioception.[30–33] Still, fabricating and assembling soft sensors with complex patterns among compliant matrices are still challenging. To address these issues, various approaches, including inserting optical waveguides into 3D-printed flexible scaffolds[23] and air-filled channels embedded within architected materials,[22] have been proposed for versatile perceptions through 3D printing. Therefore, manufacturing and arranging 3D distributed soft sensors is crucial to achieving the versatile perception of 3D external or internal stimuli.

Inspired by the receptors spatially distributed in our human bodies, we proposed a strategy for 3D stimuli perception by innervation of sensing microchannels infused with biocompatible ionic liquids, as shown in **Figure 1**. Different from existing 3D structural electronics fabricated by depositing conducting elements onto rigid surfaces,[12,34,35] the soft elastomer matrix and liquid conductor endow the receptors with excellent compliance and adaptability for human–machine interaction. The structures can be easily fabricated by soft demolding proposed in our previous work.[3] According to the resistance change of the distributed sensing microchannels, both the tactile motions and force directions can be recognized. Finally, to present the sensing ability of internal stimuli, we fabricated a soft sensorized actuator containing orthogonally distributed actuating and sensing microchannels resembling muscle fiber and proprioceptors and demonstrated its proprioception for bending, elongation, and bending direction recognition. Innervation of sensory arrays exhibits their versatile sensing ability and offers new designs for interacting with actuating elements. We also demonstrated a soft cubic sensor for external tactile motions (pressing, squeezing, shearing, and twisting) and their real-time directions (pressing faces, shearing, and twisting directions) recognizing when interacting with a human finger via a dendriform microchannel in the body diagonal and two microchannels in the face diagonal. Moreover, we employed this soft sensor as a controller for controlling the motion of the robot for the virtual reality (VR) application.

2. Results and Discussion

2.1. Fabrication of the Soft Sensors

We first fabricated a soft sensor containing a 1D sensing microchannel, as shown in **Figure 2**a. A template is first fixed into a 3D-printed mold, and then, the elastomer precursor is poured into the mold. After the elastomer is cured, it is detached from the mold. Next, the template is demolded from the elastic matrix, and the microchannel is generated. Finally, the conductive liquid is infused into the straight microchannel (diameter: 400 μm, length: 40 mm) with a round cross-section, and both ends are capped with flexible conducting wires to compose the soft sensor (Figure 2b). The uniform geometry of the round cross-section distorts less when stretched compared to rectangular cross-sections.[3] Based on the directional movement of ions under applied voltage, the potassium iodide dissolved in glycerol is chosen as the conductive liquid due to its low cost and biocompatibility.[27] This designed structure, conductive liquid encapsulated in an elastomer, endows the soft sensor with excellent flexibility and reliability to resist mechanical deformations, including bending, stretching, and twisting, as shown in Figure 2c. Moreover, the sensor containing multiple 3D microchannels can also be fabricated by a similar protocol.

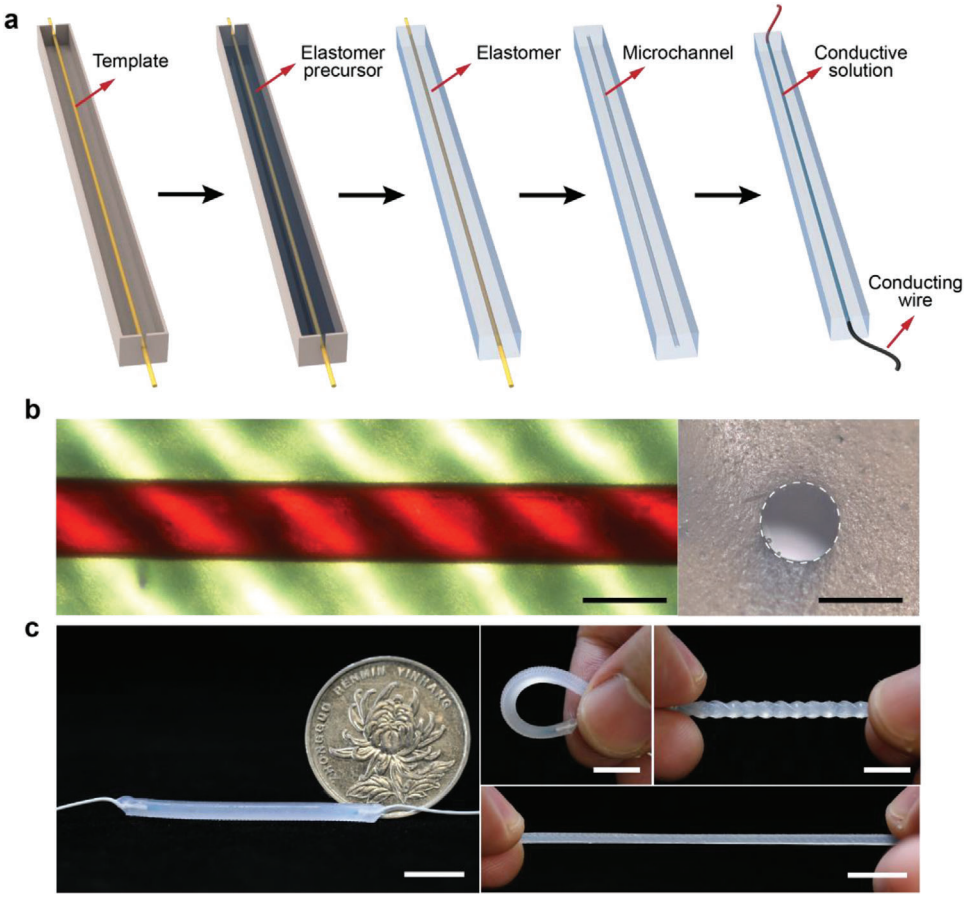

Figure 2. Soft sensor fabrication and its structure. a) Fabrication process of 1D soft sensor. A template is first fixed into a 3D-printed mold. Then, the elastomer precursor is poured into the mold. After the elastomer is cured, it is detached from the mold. Next, the template is demolded from the elastic matrix, and the microchannel is generated. Finally, the conductive liquid is injected into the microchannel, and both ends are capped with conducting wires. b) The optical image of a microchannel containing red dye and its cross-sectional geometry. Scale bar, 500 μm. c) The soft sensor under bending, twisting and stretching deformation. Scale bars, 5 mm.

2.2. Modeling and Characterization of the Soft Sensors

The resistance change of sensing microchannels under different deformations is contributed to their geometrical variances, including the length and cross-section. Therefore, quantitative analyses are conducted for resistance change prediction under different external stimuli. For the 1D sensing microchannel, the in-plane deformation (i.e., axial deformation) resulting in the resistance change $\Delta R/R_0$ is decided by:[36]

$$\frac{\Delta R}{R_0} = k\left(\epsilon^2 + 2\epsilon\right) \tag{1}$$

where ΔR is the resistance change, R_0 is the original resistance, k is the prefactor, and ϵ is the strain. To evaluate the sensing behavior of the soft sensor during unidirectional stretching, we built a stretching platform (Figure S1, Supporting Information). We tested the resistance change of soft sensors with the applied strain up to 60% under different stretch rates (50, 100, 200, and 300 mm min^{-1}), and the gauge factor of the soft sensor is 1.3 (Figure S2a, Supporting Information). The theoretical fitting curve (**Figure 3**a) for the relationship between resistance change and applied strain agrees well with our experimental results. The resistance change coincides with the applied force under 100% strain, demonstrating its low hysteresis (Figure 3b). Its small force range (0–100 mN) and small dimension present potential for wearable sensors. In addition, temperature fluctuation has drawn great concern to wearable sensors due to the calibration requirement when attaching sensors to human bodies. Herein, we conducted strain tests under different temperatures (4, 25, and 50 °C), and the resistance changed from 0.41 to 0.13 MΩ (Figure S2, Supporting Information). We observed that the resistance change and applied force show little deviation under different temperatures, especially under 40% strain (Figure S2c, Supporting Information). We also performed a cyclic test with 100% strain on the soft sensor (Figure 3d). A small change in resistance change behavior (the maximum variation less than 10%) after 300 cycles demonstrates the reliability and durability of the soft sensor.

In addition, the pressing deformation (normal to the axial direction) acting on the 1D microchannel also causes the resistance change due to the cross-sectional area variation. The finite element analysis (FEA) and experiments were performed to investigate the resistance response under pressing, and the numerical

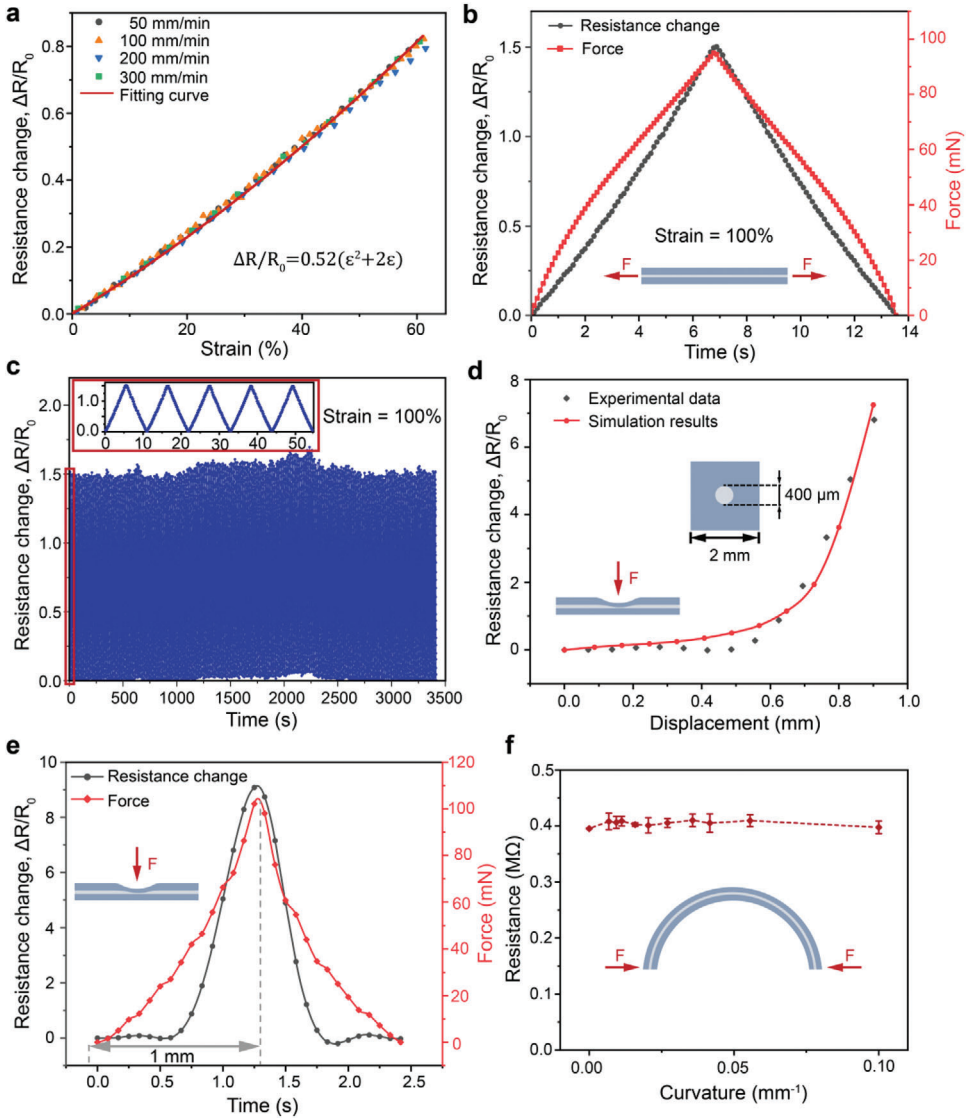

Figure 3. Characterization of the 1D soft sensor in different deformation modes. a) Experimental and theoretical results of the resistance change varying with strain under different stretch rates. b) Responses of the resistance change and applied force in one stretch cycle (100% stretch). c) Experimental results of the soft sensor's resistance change under 300 stretching cycle tests. The inset shows the first five cycles. d) Experimental and simulation results of resistance change under pressing. e) Responses of the resistance change and applied force in one pressing cycle (1.5 mm displacement). f) Experimental results of resistance as a function of curvature. The data are presented as mean values ± standard deviation with the sample size $n = 3$.

solutions fit well with our experimental results (Figure. 3d). The resistance remained constant at first. Then a sharp increment in resistance change occurs since the sensing microchannel begins to be deformed when the pressing displacement is over 0.5 mm (Figure 3e). Additionally, the response time and recovery time were measured by applying and removing a weight to the 1D soft sensor. Compared to flexible capacitive sensors,[37,38] our soft resistive sensor exhibits a slower response time (0.16 s) and recover time (0.1 s) due to the resistance change mechanism of geometry deforming and elastoviscosity of the soft matrix (Figure S3, Supporting Information). However, there is no noticeable change in resistance when the curvature changes from 0 to 0.1 mm^{-1} due to slight deformation in the length or cross-section of the sensing microchannel under measurement (Figure 3f). The pressure and bending tests were also performed (Figure S1, Supporting Information). To sum up, the 1D sensing microchannel is sensitive to stretching force along with the axial direction and pressing force normal to its axial direction. Therefore, any force applied to the sensing microchannel can be divided into two orthogonal forces: one force is along with the axial direction, and the other is normal to the axial direction, which is suitable for predicting the resistance change based on our built models.

After validating the sensing ability of the 1D soft sensor, we built a cubic soft matrix containing two 3D sensing microchannels (diameter: 400 μm) to demonstrate their sensing ability under versatile deformations. A channel in the face diagonal (Channel A) and the other in the body diagonal (Channel B) are arranged for perceiving 3D stimuli (**Figure 4**a). We built the plat-

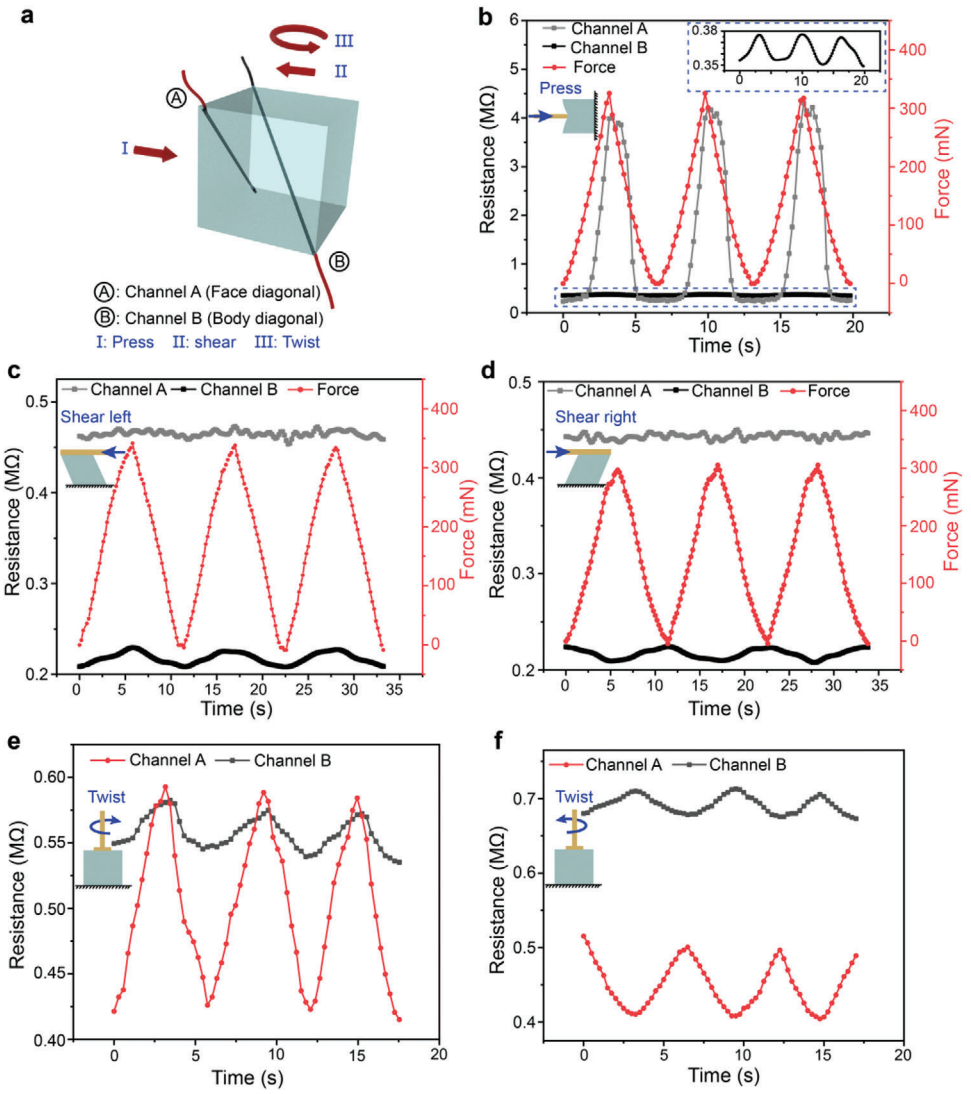

Figure 4. Characterization of the 3D sensing microchannels in different deformation modes. a) Illustration of 3D sensing microchannels under different external stimuli. b) Response of the resistance change of sensing microchannels under pressing. c,d) Responses of the resistance change of sensing microchannels under shearing in the left and right directions, respectively. e,f) Responses of the resistance change of sensing microchannels under twisting in clockwise and anticlockwise directions, respectively.

forms for the corresponding deformation tests (Figure S4, Supporting Information). When the pressure was applied to the cubic sensor by an indenter (diameter: 5 mm), Channel A showed a shape increment in resistance due to the short distance to the point load and the synergistic effect of pressing, bending, and stretching. A small increment appeared in Channel B since the applied force decays along the force direction and affects the geometry of the microchannel slightly. The resistance of Channel A increased as the shear force was applied in the left direction due to elongating this microchannel (Figure 4c). Shearing right presented an opposite electric behavior of Channel B due to shortening Channel B (Figure 4d). In contrast, Channel A is insensitive to shear deformation since this microchannel was intact during the shearing processes. Shearing front and back showed similar electric behaviors of the sensing microchannels (Figure S5, Supporting Information). When a clockwise rotation was applied to the cubic sensor, the resistances of Channel A and Channel B increased simultaneously (Figure 4e), and the higher increment of Channel A resulted from the larger elongation of the microchannel. After we inverted the rotation direction, the resistance of Channel A decreased, but the resistance of Channel B still increased, which means Channel B is insensitive to the twisting direction. Therefore, according to the quantitative tests of the designed sensing microchannels (Figure 4), the sensing microchannel in the face diagonal is sensitive to normal loads and twisting stimuli, and the microchannel in the body diagonal is sensitive to shearing stimuli. Statistical analyses were performed to present the deviation of the sensing channel response during the cyclic tests, and most data deviations fall in ±5%. Moreover, the varying tendency of channels' response and relative magnitude is coincident during cycles, which demonstrates their functionality and reliability for the following demonstrations.

2.3. Demonstration of the Soft Actuator with Intervention 3D Microchannel Network for Internal Stimuli Perception

Soft actuators are a recently emerging technique due to their adaptivity and safety,[3,39,40] but most current soft actuators lack embedded sensors to measure their deformation resulting from the large strain during operation.[41–43] Previously, adhering flexible sensors to the outer surface of soft actuators was a general approach to measuring the bending behavior of soft actuators.[44,45] Still, inextensible layers in sensors and the weak interface strength between sensors and actuators limit their applications in high-strain deformation (e.g., elongating and twisting) monitoring.[44,46,47] Embedding soft sensors into soft actuators has been employed for various soft robots recently.[22,30,32,48] Generally, these soft sensors have been applicable for large-size soft actuators or single direction bending.[32,48] Here we integrated our microchannel network into a small-scale soft actuator (10 mm × 8 mm × 50 mm) to acquire the 3D deformation, including bidirectional bending and elongating, and the comparison with existing sensors is shown in Table S1 (Supporting Information). We fabricated a soft sensorized actuator containing two actuating microchannels (diameter: 600 μm) and three sensing microchannels (diameter: 400 μm), and these interlaced microchannels for sensing and actuating of the actuator resemble our arm with innervation of proprioceptors and muscle fibers for predictable and delicate manipulations. The detailed channel structures are shown in Figure S6a (Supporting Information). Since the resistance of sensing microchannel is sensitive to stretching and pressing deformations, the orthogonally distributed of Sensor 1, 2, and Actuator i, ii are designed for inflating perception of the actuating microchannels, and Sensor 3 is designed for elongation perception of the soft sensorized actuator (**Figure 5**a). The actuation configurations of our soft actuator, including bending, elongating, and bending directions, are capable of recognizing through the distributed sensing microchannels.

Following the same protocol (Figure 2a), the soft actuator was fabricated. A pressured air control system was also built to inflate the soft actuator (Figure S7a, Supporting Information). The bending behavior of the soft actuator under different pressures for left and right bending was demonstrated in Figure 5b, and the bending angle is defined as the angle between the tangential direction of the end part of the soft actuator and the vertical direction. We first measured the electric signal response of Sensor 1 when inflating Actuator i, and the resistance of Sensor 1 increased obviously as the bending angle increased (Figure 5c). Likewise, Sensor 2 was employed to perceive Actuator ii (Figure 5d). The resistance change in Channel 3 is caused by elongating and pressing of the two actuating channels. The deviation of the response of the sensing channels results from the asymmetric location of the microchannels. In addition, to present the elongation of the soft actuator, an array of strain-limited layers (3D-printed rigid shell with 5 mm in width) were attached to the surface of the soft actuator (Figure 5e). The elongation was realized by inflating Actuator i and ii at the same flow rate simultaneously, and the displacement for the five marks in the soft actuator under different pressures was analyzed in Figure 5e. Sensor 1 and 2 detect whether the actuating channels are inflated, and Sensor 3 can measure the elongation of the soft actuator under the deformation of both elongating and pressing (Figure 5f; Video S1, Supporting Information). The cyclic tests for right bending and elongating of the sensorized actuators were also performed under corresponding sensing channel recording to demonstrate their reliability and repeatability (Figure S7, Supporting Information). Through the interaction between actuating and sensing microchannels distributed in the soft actuator, the internal stimuli, including deformation types (bending and elongating), magnitudes (bending angles and elongation), and directions (bending directions), could be identified (Video S1, Supporting Information).

2.4. Demonstration of the Sensor Containing a 3D Microchannel Network for External Stimuli Perception

External stimuli perception is crucial to our human beings and robots for interacting with unknown environments safely and achieving dexterous manipulation controllably. The ability of 3D external stimuli perception, such as force types (e.g., pressing, shearing, and twisting) and force directions, endows soft robotics and wearable devices with more versatile manipulations. Electronic skins are the most popular solution to external stimuli perception. Not only tactile motions and real-time directions but temperature variation can be recognized through the designed sensing structures and specific materials.[19,49,50] However, their complicated fabrication processes and planar geometries are not applicable to 3D external stimuli perception of 3D soft machines. Inspired by the innervation of sensory receptors in our skin, we fabricated a hierarchically structured 3D microchannel network (diameter: 400 μm), including a dendriform microchannel in the body diagonal and two microchannels in the face diagonal, into an elastic matrix for external stimuli perception (**Figure 6**a), based on our previous results (Figure 4). The detailed channel structures are shown in Figure S6b (Supporting Information). The two microchannels in the face diagonal are employed to measure the side pressing force and twisting force with directions. To demonstrate the fabrication capacity of our approach, reduce the number of conducting wires (from eight to five) employed in the sensor, and increase the top-face pressing sensing ability by reducing the distance between the channels and applied force, we employed a dendriform microchannel in the body diagonal here. By identifying the corresponding resistance variance modes of the multiple sensing microchannels that are distributed in different locations and attitudes, this soft cubic sensor can recognize different types of stimuli and real-time directions, resembling the functionality of human skin.

The soft cubic sensor with a spatially distributed microchannel network was fabricated (Figure S8a, Supporting Information). Saturated potassium iodide-glycerol was injected into the microchannels to work as a conductor, connected in series to a resistor (3 MΩ). A 5 V DC voltage was applied to the circuit, and the voltage on each microchannel was measured by a data acquisition (DAQ) board (TB-4309, NI) (Figure S8b, Supporting Information). The cubic sensor was capable of identifying the force types and real-time directions acting on the cubic matrix through the microchannels' different electrical response patterns (Figure 6a). This capability was based on the different deformation sensitivities of the sensing microchannels, which were located in different parts of the sensor: two (Channels 1 and 2) on the surfaces and

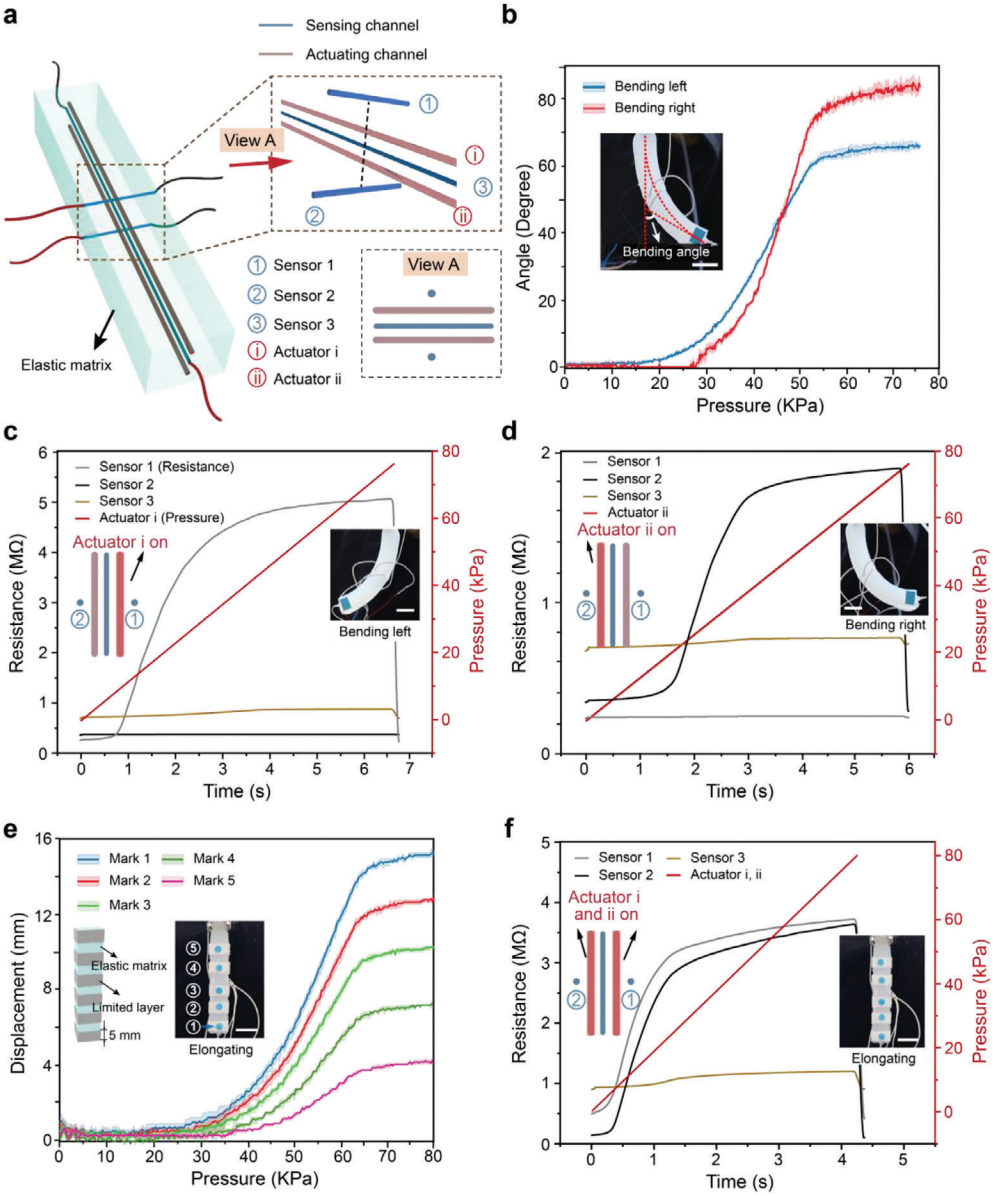

Figure 5. Demonstration of the sensorized soft actuators for internal stimuli perception. a) Schematic diagram and channel distribution of the actuator, including three sensing channels and two actuating channels. b) The response of bending angle under different pressures for left and right bending. c,d) Responses of the resistance change of sensing channels with the pressure increasing for the left and right bending of the actuator, respectively. e) The response of elongation under different pressures of five individual marks. f) The response of the resistance change of sensing channels with the pressure increasing for the elongating of the soft actuator with segmented strain-limited layers. Scale bar, 1 cm. The data in (b) and (e) are presented as mean values ± standard deviation with the sample size $n = 3$.

the other four (Channels 3–6) in the body. As shown in Figure 6a and Video S2 (Supporting Information), all the resistances of the microchannels increased when a normal force was applied (Stimulus I, II, and III). In contrast, the resistances of some pairs of channels (e.g., Channels 3 and 6, Channels 4 and 5) presented an opposite electric response that was lateral to the surfaces (Stimulus IV and V). The twisting stimuli (Stimulus VI and VII) were recognized by the same electric response of the three pairs of microchannels, Channels 1 and 2, Channels 3 and 6, and Channels 4 and 5. In addition, the relative magnitude of resistance change could be used for recognizing force directions. The press force on the top surface caused a larger resistance increment on Channels 3–6 than on the other channels, and Channel 2 showed the largest increment when squeezing the right and left faces. Moreover, the redundant sensing microchannels (Channels 4 and 5) improved the accuracy of stimuli detection. Moreover, we applied our cubic sensor to the VR interface for working as a controller due to the abundant sensibility for versatile external stimuli. We endowed the channel's responses under different stimuli (Stimulus I–VII) with corresponding order for controlling the robot's motion in the interface of Unity (version: 2020.3.40f1). For example, when applying Stimulus I to the cubic sensor, the robot jumps since

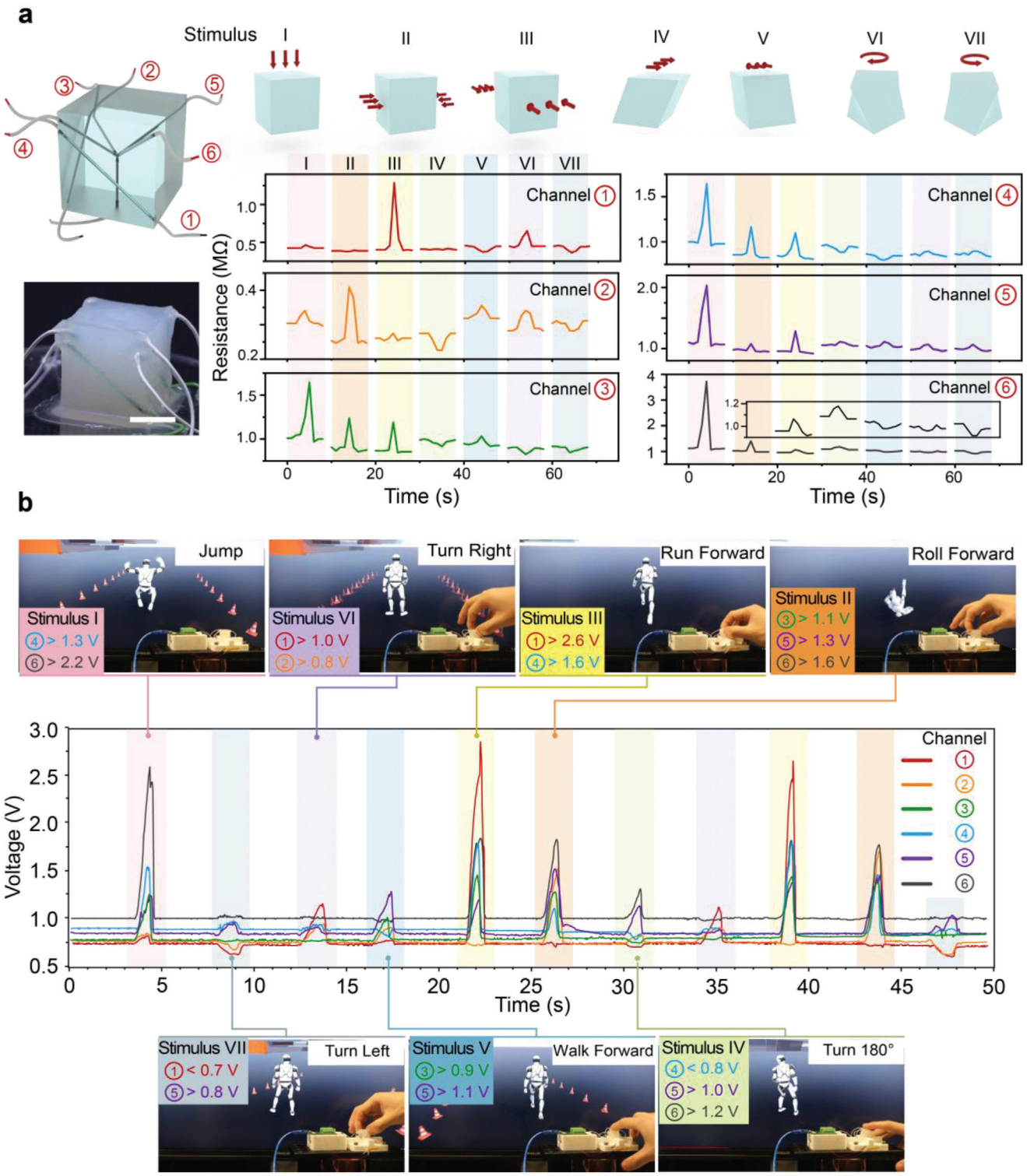

Figure 6. Demonstration of the soft cubic sensor for the external stimuli perception and VR application. a) Schematic diagram and real image of the sensor, and the response of the resistance change of the soft sensor to seven different external stimuli, including force types and force directions. Scale bar, 5 mm. b) The VR application of the sensor for the Robot's motion control according to the channel responses recognition.

the pressing causes the voltage change in Channel 4 (larger than 1.3 V), and Channel 6 (larger than 2.2 V) is defined as the jump order. According to the voltage response of different channels, we recognized the seven stimuli to control the Robot for achieving corresponding motions, including motion types (jumping, rolling, running, and walking) and moving directions (Figure 6b; Figure S8 and Video S3, Supporting Information). Our soft cubic sensor demonstrated the innervation of sensing microchannels for 3D external stimuli perception, including pressing, squeezing, shearing, and twisting forces and their real-time directions. The VR application of the cubic sensor is also realized.

3. Conclusion

In this work, we demonstrated 3D distributed sensing microchannel networks embedded into elastic matrices to mimic the exteroception and proprioception of human bodies for external and internal stimuli perception. We first fabricated and characterized 1D sensing microchannels under different physical stimuli and realized the microchannels are sensitive to stretching and pressing. Then, 3D microchannels distributed in the face diagonal and body diagonal of a soft cubic matrix were fabricated for 3D external stimuli perception, including pressing, shearing, and twisting, and concluded that the microchannel in the face diagonal is sensitive to pressing and twisting, and microchannel in the body diagonal is sensitive to shearing and twisting. Finally, we demonstrated a soft sensorized actuator could recognize the deformation configurations (bending, elongating, and bending directions) and magnitudes (bending angle and elongation) of the soft actuator based on the response of resistance in the sensing microchannels. We also demonstrated a soft cubic sensor containing a dendriform microchannel in the body diagonal and two microchannels in the face diagonal was capable of identifying 3D external stimuli, including force types (pressing, squeezing, shearing, and twisting) and real-time directions via measuring the corresponding resistance variance modes and their relative magnitude. In addition, the VR application of the cubic sensor is also achieved by endowing the channel's responses with the corresponding motions of the robot in the VR interface.

The demonstrations of the soft sensorized actuator and soft cubic sensor are just two simple prototypes for 3D stimuli perception based on our new approach, embedding 3D sensing microchannels into elastic matrices. Our sensing microchannels present intriguing demonstrations in soft actuators and human–machine interactions (i.e., VR applications), and we believe our new approach could be involved in tremendous potential applications for improving perception spinning wearable devices, soft robotics, and medical devices in the future. In addition, based on the orthogonal distribution of soft sensors and actuating channels, the spatial resolution can be realized by distributing arrays of the designed 3D microchannels into the corresponding bodies, and in combination with machine learning, the accuracy and response speed of stimuli recognition can be improved. Theoretical model building for 3D sensing channels could improve their accuracy of strain and force for various deformation measurements. Functional materials could also be employed for broader sensing abilities, including temperature,[19] humidity,[49] and biomarkers[51] in the future.

4. Experimental Section

Preparation of Conductive Solution: Excess potassium iodide (8 g, Macklin) was dissolved into glycerol (20 mL, Energy Chemical) in a vial and stirred overnight by a magnetic stirrer (MR Hei-Tech) at room temperature. Finally, the supernatant solution was extracted for later usage.

Fabrication of the 1D Soft Sensor: A filiform template (400 µm, TPU 95-A, eSUN) was prepared by extruding from a 3D printer nozzle. Then, this template was fixed into a 3D-printed mold. Next, the elastomer precursor was prepared by adding part A and part B of Ecoflex 0030 precursor into a cup with equal volume, stirring for 1 min, and vacuuming for 4 min to degas. Later, the prepared elastomer precursor was poured into the mold. After the elastomer was cured, it was detached from the mold. Next, the template was demolded from the elastic matrix, and the microchannel was generated. Finally, the prepared conductive liquid was injected into the microchannel by a medical syringe, and both ends were capped with flexible conducting wires, as shown in Figure 2a.

Strain Sensing Tests of the 1D Soft Sensor: Strain sensing tests were performed by the designed platform (Figure S2a, Supporting Information). Both ends of the sensor were fixed to the supports, which were connected to the sliding stage, and the sensor was stretched with different stretch rates (50, 100, 200, and 300 mm min^{-1}) at room temperature. Five cycles were conducted for each stretch rate.

The sensor was tested in three temperature conditions (4, 25, and 50 °C) to test the effect on the sensing ability. The testing setup and sensor were placed in a refrigerator (4 °C), an oven (50 °C), and room temperature (25 °C) in sequence and waited for 20 min before tests.

Bending Sensing Tests of 1D Soft Sensor: The soft sensor bending sensing ability was tested by conformally attaching the sensor to 10 cylindrical objects with different curvatures. The test was repeated three times for each curvature test.

Simulation of the Pressing Process for the 1D Soft Sensor: A finite element analysis model (ABAQUS Explicit 2020) was built for quasi-static analysis of the deforming process. The 3D model was simplified into a 2D symmetric planar stress model with the full quadrilateral meshes (mash size: 0.05 mm). The materials were set as hyper-elastic with the quadratic polynomial constitutive model, and the parameters were generated from a realistic compression test. The compressing process was performed by setting the symmetry constraints and displacement loads on the top and bottom surfaces to acquire the change in the cross-sectional area of the microchannels. The channel's area was calculated by integrating after obtaining the boundary conditions of the microchannel at each sub-step of time. Finally, the relationship between the pressing displacement and the cross-sectional area change of the microchannel was obtained.

Pressure Sensing Tests of the 1D Soft Sensor: The pressure sensing tests were performed by the designed platform (Figure S2b, Supporting Information). The bottom of the 1D soft sensor was glued to the vertical substrate of the mold by a silicone glue (SIL-Poxy, Smooth-On), and an indenter, whose tip is in a semicircular cylinder (diameter: 1 mm), was employed to press the soft sensor with 1 mm displacement at the speed of 50 mm min^{-1} and repeated five cycles.

Response Time and Recovery Time Measurement under Pressing: The 1D soft sensor was connected to an oscilloscope (Tektronix, MSO024) for measuring the voltage variation during the measurement. A heavy weight (100 g) was applied onto the soft sensor to generate a quick compression. After holding for 10 s, the weight was removed from the sensor quickly. The result is shown in Figure S3 (Supporting Information).

Pressure Sensing Tests of the Cubic Soft Sensor Containing Two Sensing Microchannels: The pressure sensing tests were performed by the designed platform (Figure S4a, Supporting Information). The bottom of the cubic soft sensor was glued to the vertical substrate, and an indenter with a tip in hemispherical geometry (diameter: 5 mm) was employed to apply pressure onto the distrusted sensing microchannels. During the tests, the indenter advancing 3 mm and returning at the speed of 50 mm min^{-1} was a pressure cycle. Five cycles were conducted for the pressure test.

Shear Sensing Tests of the Cubic Soft Sensor Containing Two Sensing Microchannels: The shear sensing tests were performed by the designed platform (Figure S4b, Supporting Information). The bottom of the cubic

soft sensor was glued to the substrate, and a precompression of 1 mm displacement was applied to the cubic sensor to avoid slipping between the sensor and the shear plate. The shear tests were performed in the left and right directions (Figure 4a) at the speed of 50 mm min^{-1}, and the shear displacement was 5 mm. Five cycles were conducted for each shear test.

Twist Sensing Tests of the Cubic Soft Sensor Containing Two Sensing Microchannels: The twist sensing tests were performed by the designed platform (Figure S4c, Supporting Information). The bottom of the cubic soft sensor was glued to the substrate, and a precompression of 1 mm displacement was applied to the top of the cubic sensor by a rotational plate. The twist tests were performed clockwise and anticlockwise (Figure 4a) at the rotational speed of 7.5° s^{-1}, and the rotation degree was 45°. Five cycles were conducted for each twist test.

Cyclic Tests for the Sensorized Soft Actuators: For bending and elongating tests, the pressured air pipeline was connected to the corresponding actuating channel, and a proportional valve was employed to apply a linear increasing pressure pulse to the actuator and then depressurized to 0 kPa suddenly. A 2 s time interval exists between each cycle (Figure S7c, Supporting Information). Four different pressures were applied to the bending and elongating deformations, respectively, and over ten cycles were repeated under each pressure. Sensor 2 was employed to record the right bending, and Sensor 3 was employed to record the elongating.

Statistical Analysis: All data in this work were collected without preprocessing and presented as the mean ± standard deviation. The sample size *n* for each experiment was at least three and had been indicated where applicable. To analyze the 3D sensing channel response data, the rising edge data from different sensing behaviors into groups were taken. A column of data from each data group as the benchmark data and the error of the other two comparative data columns in this group relative to the benchmark data were selected. The deviation was calculated by: (comparative data − benchmark data)/benchmark data. Software used for data analysis included Origin and MATLAB.

Supporting Information

Supporting Information is available from the Wiley Online Library or from the author.

Acknowledgements

D.F. and R.Z. contributed equally to this work. This work was in part funded by the National Natural Science Foundation of China (52275021, H.W.), the National Key R&D Program of China (2022YFB4701200, H.W.), the Science, Technology, and Innovation Commission of Shenzhen Municipality (ZDSYS20200811143601004, H.W.), the Natural Science Foundation of Liaoning Province of China (State Key Laboratory of Robotics joint funding, 2021-KF-22-11, H.W.), the Southern Marine Science and Engineering Guangdong Laboratory (Guangzhou) (K19313901, H.W.). The authors acknowledge the assistance of SUSTech Core Research Facilities.

Conflict of Interest

The authors declare no conflict of interest.

Data Availability Statement

The data that support the findings of this study are available in the Supporting Information of this article.

Keywords

soft sensors, 3D sensing microchannels, sensor designs, exteroception and proprioception

Received: March 3, 2023
Published online:

[1] M. Wang, Y. Luo, T. Wang, C. Wan, L. Pan, S. Pan, K. He, A. Neo, X. Chen, *Adv. Mater.* **2021**, *33*, 2003014.
[2] J. C. Tuthill, E. Azim, *Curr. Biol.* **2018**, *28*, R194.
[3] D. Fan, X. Yuan, W. Wu, R. Zhu, X. Yang, Y. Liao, Y. Ma, C. Xiao, C. Chen, C. Liu, *Nat. Commun.* **2022**, *13*, 5083.
[4] Z. Song, Z. Fu, D. Romano, P. Dario, J. S. Dai, *Soft Rob.* **2022**, *9*, 440.
[5] K. P. Becker, Y. Chen, R. J. Wood, *Adv. Funct. Mater.* **2020**, *30*, 1908919.
[6] H. Wang, P. York, Y. Chen, S. Russo, T. Ranzani, C. Walsh, R. J. Wood, *Int. J. Rob. Res.* **2021**, *40*, 895.
[7] H. Bai, S. Li, J. Barreiros, Y. Tu, C. R. Pollock, R. F. Shepherd, *Science* **2020**, *370*, 848.
[8] J. S. Marion, N. Gupta, H. Cheung, K. Monir, P. Anikeeva, Y. Fink, *Adv. Mater.* **2022**, *34*, 2201081.
[9] Y. Ji, Y. Liao, H. Li, Y. Cai, D. Fan, Q. Liu, S. Huang, R. Zhu, S. Wang, H. Wang, *ACS Appl. Mater. Interfaces* **2022**, *14*, 11971.
[10] Y. Fu, H. Wang, Y. Zi, X. Liang, *Nano Energy* **2021**, *89*, 106368.
[11] J. Kim, M. Lee, H. J. Shim, R. Ghaffari, H. R. Cho, D. Son, Y. H. Jung, M. Soh, C. Choi, S. Jung, *Nat. Commun.* **2014**, *5*, 5747.
[12] R. Hensleigh, H. Cui, Z. Xu, J. Massman, D. Yao, J. Berrigan, X. Zheng, *Nat. Electron.* **2020**, *3*, 216.
[13] L. Cai, S. Zhang, Y. Zhang, J. Li, J. Miao, Q. Wang, Z. Yu, C. Wang, *Adv. Mater. Technol.* **2018**, *3*, 1700232.
[14] G. Gu, N. Zhang, H. Xu, S. Lin, Y. Yu, G. Chai, L. Ge, H. Yang, Q. Shao, X. Sheng, *Nat. Biomed. Eng.* **2021**, https://doi.org/10.1038/s41551-021-00767-0
[15] Y. Mengüç, Y.-L. Park, H. Pei, D. Vogt, P. M. Aubin, E. Winchell, L. Fluke, L. Stirling, R. J. Wood, C. J. Walsh, *Int. J. Rob. Res.* **2014**, *33*, 1748.
[16] J. Park, Y. Lee, J. Hong, Y. Lee, M. Ha, Y. Jung, H. Lim, S. Y. Kim, H. Ko, *ACS Nano* **2014**, *8*, 12020.
[17] M. S. Sarwar, Y. Dobashi, C. Preston, J. K. Wyss, S. Mirabbasi, J. D. W. Madden, *Sci. Adv.* **2017**, *3*, e1602200.
[18] B. Shih, D. Shah, J. Li, T. G. Thuruthel, Y.-L. Park, F. Iida, Z. Bao, R. Kramer-Bottiglio, M. T. Tolley, *Sci. Rob.* **2020**, *5*, 9239.
[19] I. You, D. G. Mackanic, N. Matsuhisa, J. Kang, J. Kwon, L. Beker, J. Mun, W. Suh, T. Y. Kim, J. B.-H. Tok, *Science* **2020**, *370*, 961.
[20] C. M. Boutry, M. Negre, M. Jorda, O. Vardoulis, A. Chortos, O. Khatib, Z. Bao, *Sci. Rob.* **2018**, *3*, 6914.
[21] M. Han, L. Chen, K. Aras, C. Liang, X. Chen, H. Zhao, K. Li, N. R. Faye, B. Sun, J.-H. Kim, *Nat. Biomed. Eng.* **2020**, *4*, 997.
[22] R. L. Truby, L. Chin, A. Zhang, D. Rus, *Sci. Adv.* **2022**, *8*, 4385.
[23] P. A. Xu, A. K. Mishra, H. Bai, C. A. Aubin, L. Zullo, R. F. Shepherd, *Sci. Rob.* **2019**, *4*, 6304.
[24] T. G. Thuruthel, B. Shih, C. Laschi, M. T. Tolley, *Sci. Rob.* **2019**, *4*, 1488.
[25] J. C. Yeo, J. Yu, Z. M. Koh, Z. Wang, C. T. Lim, *Lab Chip* **2016**, *16*, 3244.
[26] D. M. Vogt, Y.-L. Park, R. J. Wood, *IEEE Sens. J.* **2013**, *13*, 4056.
[27] S. Xu, D. M. Vogt, W. H. Hsu, J. Osborne, T. Walsh, J. R. Foster, S. K. Sullivan, V. C. Smith, A. W. Rousing, E. C. Goldfield, *Adv. Funct. Mater.* **2019**, *29*, 1807058.
[28] T. Kim, Y.-L. Park, *IEEE Robot. Autom. Lett.* **2018**, *3*, 881.
[29] D. Fan, Y. Liao, W. Wu, P. Zhang, X. Yang, R. Zhu, Y. Wang, C. Yang, H. Wang, *Adv. Mater. Technol.* **2023**, https://doi.org/10.1002/admt.202201640
[30] H. Zhao, K. O'Brien, S. Li, R. F. Shepherd, *Sci. Rob.* **2016**, *1*, 7529.
[31] T. Kim, S. Lee, T. Hong, G. Shin, T. Kim, Y.-L. Park, *Sci. Rob.* **2020**, *5*, 6878.
[32] R. L. Truby, M. Wehner, A. K. Grosskopf, D. M. Vogt, S. G. Uzel, R. J. Wood, J. A. Lewis, *Adv. Mater.* **2018**, *30*, 1706383.

[33] R. L. Truby, C. Della Santina, D. Rus, *IEEE Robot. Autom. Lett.* **2020**, *5*, 3299.
[34] D. Espalin, D. W. Muse, E. MacDonald, R. B. Wicker, *Int. J. Adv. Manuf. Technol.* **2014**, *72*, 963.
[35] M. Kaur, T. H. Kim, W. S. Kim, *Adv. Mater.* **2021**, *33*, 2002534.
[36] R. Matsuzaki, K. Tabayashi, *Adv. Funct. Mater.* **2015**, *25*, 3806.
[37] S. Lee, A. Reuveny, J. Reeder, S. Lee, H. Jin, Q. Liu, T. Yokota, T. Sekitani, T. Isoyama, Y. Abe, *Nat. Nanotechnol.* **2016**, *11*, 472.
[38] Y. Zhang, J. Yang, X. Hou, G. Li, L. Wang, N. Bai, M. Cai, L. Zhao, Y. Wang, J. Zhang, *Nat. Commun.* **2022**, *13*, 1317.
[39] G. M. Whitesides, *Angew. Chem., Int. Ed.* **2018**, *57*, 4258.
[40] R. Zhu, D. Fan, W. Wu, C. He, G. Xu, J. S. Dai, H. Wang, *Adv. Intell. Syst.* **2023**, https://doi.org/10.1002/aisy.202200301
[41] Y. Cui, X.-J. Liu, X. Dong, J. Zhou, H. Zhao, *IEEE Trans. Robot.* **2021**, *37*, 1604.
[42] T. J. Jones, E. Jambon-Puillet, J. Marthelot, P.-T. Brun, *Nature* **2021**, *599*, 229.
[43] D. Li, D. Fan, R. Zhu, Q. Lei, Y. Liao, X. Yang, Y. Pan, Z. Wang, Y. Wu, S. Liu, *Soft Rob.* **2022**, https://doi.org/10.1089/soro.2021.0185
[44] T. Jin, Z. Sun, L. Li, Q. Zhang, M. Zhu, Z. Zhang, G. Yuan, T. Chen, Y. Tian, X. Hou, *Nat. Commun.* **2020**, *11*, 5381.
[45] Q. Zou, Y. Wang, F. Yang, *Sens. Actuators, A* **2021**, *332*, 113084.
[46] G. Gerboni, A. Diodato, G. Ciuti, M. Cianchetti, A. Menciassi, *IEEE ASME Trans. Mechatron.* **2017**, *22*, 1881.
[47] R. A. Bilodeau, M. C. Yuen, J. C. Case, T. L. Buckner, R. Kramer-Bottiglio, presented at *2018 IEEE/RSJ International Conference on Intelligent Robots and Systems (IROS)*, IEEE, Madrid, Spain **2018**.
[48] L. Somm, D. Hahn, N. Kumar, S. Coros, *IEEE Robot. Autom. Lett.* **2019**, *4*, 761.
[49] Q. Hua, J. Sun, H. Liu, R. Bao, R. Yu, J. Zhai, C. Pan, Z. L. Wang, *Nat. Commun.* **2018**, *9*, 244.
[50] G. Y. Bae, J. T. Han, G. Lee, S. Lee, S. W. Kim, S. Park, J. Kwon, S. Jung, K. Cho, *Adv. Mater.* **2018**, *30*, 1803388.
[51] T. Someya, M. Amagai, *Nat. Biotechnol.* **2019**, *37*, 382.